PHYSICS LETTERS B

Letter

Visualizing quantum coherence and decoherence in nuclear reactions

K. Hagino [ID],*, T. Yoda [ID]

Department of Physics, Kyoto University, Kyoto 606-8502, Japan

ARTICLE INFO

ABSTRACT

Differential cross sections of nuclear reactions often exhibit characteristic oscillations in the angular distribution originated from an interference of two indistinguishable processes. Here we propose a novel method to visualize origins of such oscillations. This is achieved by taking Fourier transform of scattering amplitudes, following the idea in wave optics. We apply this method to elastic scattering of $^{16}O+^{16}O$ and $^{18}O+^{18}O$ at energies above the Coulomb barrier. The former system shows strong oscillations in the angular distribution due to the nearside-farside interferences, while the oscillations are largely suppressed in the latter system due to a stronger absorption. We show that the images of the former and the latter systems correspond to a double-slit and a single-slit problems in quantum mechanics, respectively.

In quantum mechanics, when two or more indistinguishable processes are involved, the probability is computed by taking the absolute square of the total amplitude, which is given as a sum of the amplitude of each process. This leads to the interference of each process due to the cross terms. This is referred to as quantum coherence, and this is one of the most fundamental features of quantum mechanics. In addition to the famous double-slit problem, a textbook example for this is scattering of two identical particles, for which a detector cannot distinguish scattering at angle θ from scattering at angle $\pi - \theta$. In this case, the differential cross sections are given by $d\sigma/d\Omega = |f(\theta) \pm f(\pi - \theta)|^2$, where $f(\theta)$ and $f(\pi - \theta)$ are scattering amplitudes for the angles θ and $\pi - \theta$, respectively, and the sign of the superposition depends on the statistics of the particles. Due to the interference between $f(\theta)$ and $f(\pi - \theta)$, the differential cross sections exhibit characteristic oscillations as a function of the scattering angle θ. Such oscillations have been actually observed e.g., in elastic scattering of $^{16}O+^{16}O$ at energies below the Coulomb barrier [1]. At such energies, the nuclear effect can be neglected, and the experimental data can be well accounted for by taking a superposition of the Rutherford scattering amplitudes at θ and $\pi - \theta$.

Besides the interference due to the exchange of two identical particles, there are many other interference phenomena known in low-energy nuclear reactions. These include, the Coulomb-nuclear interference [2], the nearside-farside interference [3–5], and the barrier-wave-internal-wave interference [6]. In particular, an analogy between the nearside-farside interference and the double-slit problem has been discussed in Ref. [5]. Here, the nearside component corresponds to scattering at a positive scattering angle with a positive impact parameter

while the farside component corresponds to scattering with a negative impact parameter. Due to a strong absorption inside a nucleus, scattering takes place only at the edge of a nucleus, which corresponds to scattering through two slits in a double slit problem.

In this paper, we propose a novel way to visualize an origin of oscillations in the angular distribution of nuclear reactions. The idea of this method is to take Fourier transform of a scattering amplitude, similar to what is done in wave optics. A similar method has been applied in particle physics, in which the images of string scattering [7] and that of black holes in the AdS/CFT correspondence [8,9] have been discussed. In particular, it has been demonstrated that the image of string scattering corresponds to a double slit [7]. With a similar motivation to that of Ref. [7], we here apply the method to elastic scattering of $^{16}O+^{16}O$ and $^{18}O+^{18}O$ at energies above the Coulomb barrier, and show how the quantum coherence in $^{16}O+^{16}O$ is decohered in $^{18}O+^{18}O$ by nuclear absorption.

Following Ref. [7], we take an image of scattering using a lens located at the direction (θ_0, φ_0) from the scattering center. To this end, we take Fourier transform of scattering amplitude in a form of

$$\Phi(X,Y) = \frac{1}{S} \int_{\theta_0-\Delta\theta}^{\theta_0+\Delta\theta} d\theta\, e^{ik(\theta-\theta_0)X} f(\theta) \int_{\varphi_0-\Delta\varphi}^{\varphi_0+\Delta\varphi} d\varphi\, e^{ik(\varphi-\varphi_0)Y}, \qquad (1)$$

where (X,Y) is the coordinate on the virtual screen behind the lens and k is the wave number, $k = \sqrt{2\mu E/\hbar^2}$, μ and E being the reduced mass and the energy in the center of mass frame, respectively. See Ap-
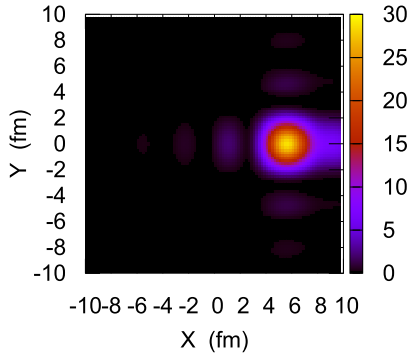
Fig. 1. The image of Rutherford scattering for $^{16}O + ^{16}O$ at $E_{c.m.} = 8.8$ MeV with the unsymmetrized Coulomb scattering amplitude. The angles in Eq. (1) are set to be $\theta_0 = 90$ degrees and $\Delta\theta = \Delta\varphi = 30$ degrees.

pendix A for a derivation of this formula. We have assumed that the scattering amplitude f is independent of the angle φ. In Eq. (1), S is the angular area of the lens given by

$$S = \int_{\theta_0-\Delta\theta}^{\theta_0+\Delta\theta} d\theta \int_{\varphi_0-\Delta\varphi}^{\varphi_0+\Delta\varphi} d\varphi = 4(\Delta\theta)(\Delta\varphi). \tag{2}$$

The actual image is given by $I(X,Y) = |\Phi(X,Y)|^2$. In this paper, following Ref. [7], we take $\Delta\varphi = \Delta\theta/\sin\theta_0$, that corresponds to a square lens.

Since the scattering amplitude does not depend on the angle φ, the Y direction of the image $I(X,Y)$ does not provide any useful information. Nevertheless, we prefer to keep a two-dimensional image, as it can be extended to a more general case where a scattering amplitude depends both on θ and φ. For a φ-independent scattering amplitude, $f(\theta)$, the integral for φ is trivial in Eq. (1) and is given by

$$\int_{\varphi_0-\Delta\varphi}^{\varphi_0+\Delta\varphi} d\varphi\, e^{ik(\varphi-\varphi_0)Y} = 2\Delta\varphi\, \frac{\sin(kY\Delta\varphi)}{kY\Delta\varphi}. \tag{3}$$

This function is peaked at $Y = 0$ and has a width of $2\pi/(k\Delta\varphi)$ [7]. The resolution of the image in the Y direction is thus determined by the quantity $k\Delta\varphi$. Notice that Eq. (3) is independent of φ_0. For a flat angular distribution with $f(\theta) = \text{const.}$, the same argument holds for the position and the resolution of the peak in the X direction.

Let us first apply Eq. (1) to Rutherford scattering, that is, scattering with a pure Coulomb potential, $V(r) = Z_1 Z_2 e^2/r$, where Z_1 and Z_2 are atomic numbers of two colliding nuclei, for which the scattering amplitude $f(\theta)$ is known analytically, see e.g. Ref. [10]. Fig. 1 shows the image of Rutherford scattering for $^{16}O + ^{16}O$ at $E_{c.m.} = 8.8$ MeV. Even though this is a system with identical bosons, the symmetrization of the wave function is not taken into account here in order to investigate an image of pure Rutheford scattering. For the image, we take $\theta_0 = 90$ degrees with $\Delta\theta = \Delta\varphi = 30$ degrees. One can see that the image has a peak at $X = 5.65$ fm. This is actually close to the classical impact parameter for Rutherford scattering of this system at $\theta_0 = 90$ degree, $b_{cl} = 5.24$ fm. As we derive in Appendix B, for Rutherford scattering the peak of the image indeed coincides with the classical impact parameter in the limit of $\Delta\theta \to 0$. We expect that this holds in general for heavy-ion reactions, for which the Coulomb interaction plays an important role in determining the reaction dynamics.

Notice that Eq. (1) for $\theta_0 = \pi/2$ has a property that $\Phi(X,Y)$ with $f(\pi-\theta)$ is identical to $\Phi(-X,Y)$ with $f(\theta)$. Therefore the image of $^{16}O + ^{16}O$ scattering with the symmetrized scattering amplitude $f(\theta) + f(\pi-\theta)$ has two symmetric peaks at X_{peak} and $-X_{peak}$, just as in the double-slit problem discussed in Ref. [7]. See the Appendix C for details.

Let us next discuss elastic scattering of $^{16}O + ^{16}O$ and $^{18}O + ^{18}O$ at energies above the Coulomb barrier, at which both the Coulomb and
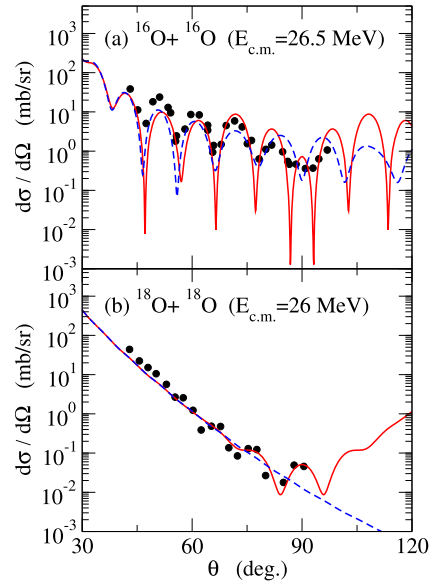

Fig. 2. (the upper panel) The angular distribution of the $^{16}O + ^{16}O$ elastic scattering at $E_{c.m.} = 26.5$ MeV. The solid line shows a fit with a deep squared Woods-Saxon potential, while the dashed line shows the unsymmetrized cross sections obtained with the same potential. The experimental data are taken from Ref. [11]. (the lower panel) The same as the upper panel, but for the $^{18}O + ^{18}O$ elastic scattering at $E_{c.m.} = 26$ MeV. The surface imaginary potential is also added to the optical potential. The experimental data are taken from Ref. [12].

the nuclear interactions play a role. The upper panel of Fig. 2 shows the angular distribution of $^{16}O + ^{16}O$ elastic scattering at $E_{c.m.} = 26.5$ MeV [11]. With a standard global nuclear potential, the height of the Coulomb barrier for this system is estimated to be around 10.3 MeV, and thus this energy is about 2.6 times the barrier height. The experimental angular distributions for this system show a strong oscillatory pattern. We fit this with a deep squared Woods-Saxon potential for the nuclear part of internucleus potential [13,14],

$$V_N(r) = -V_0\, g(R_R, a_R, r)^2 - iW_0\, g(R_W, a_W, r)^2, \tag{4}$$

with

$$g(R, a, r) = 1/(1 + \exp[(r-R)/a]). \tag{5}$$

The solid line in the upper panel is obtained with the parameters $V_0 = 421.28$ MeV, $R_R = 4.12$ fm, $a_R = 1.52$ fm, $W_0 = 157.1$ MeV, $R_W = 4.39$ fm, and $a_W = 0.151$ fm, together with the radius of the uniform charge distribution of 5.54 fm. The observed oscillations are reasonably well accounted for with this parameter set. The lower panel of Fig. 2 shows the angular distribution for the $^{18}O + ^{18}O$ at a similar energy as the one shown in the upper panel for $^{16}O + ^{16}O$ [12]. For this system, the oscillatory pattern is much less pronounced (see also Ref. [15]), and the same squared Woods-Saxon potential as that for the $^{16}O + ^{16}O$ system does not fit well the experimental data. This is most likely due to the two extra neutrons outside the doubly magic ^{16}O nucleus, with which the ^{18}O nuclei are excited more easily than the ^{16}O nuclei. A stronger absorption is necessary to fit the data [16,17], and for this purpose we introduce a surface imaginary potential,

$$W_S(r) = -iW_s\, dg(R_s, a_s, r)/dr. \tag{6}$$

The solid line in the lower panel is obtained with the parameters $W_s = 94.01$ MeV, $R_s = 5.61$ fm, and $a_s = 0.734$ fm, together with the potential given by Eq. (4) with a scaling of R_R and R_W by a factor of 1.04 to account for the mass number dependence of the nuclear radii. One can see that this calculation well accounts for the data for the $^{18}O + ^{18}O$ system. Notice that the average differential cross sections
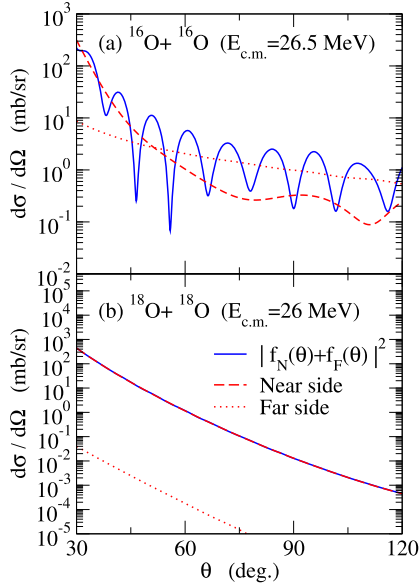
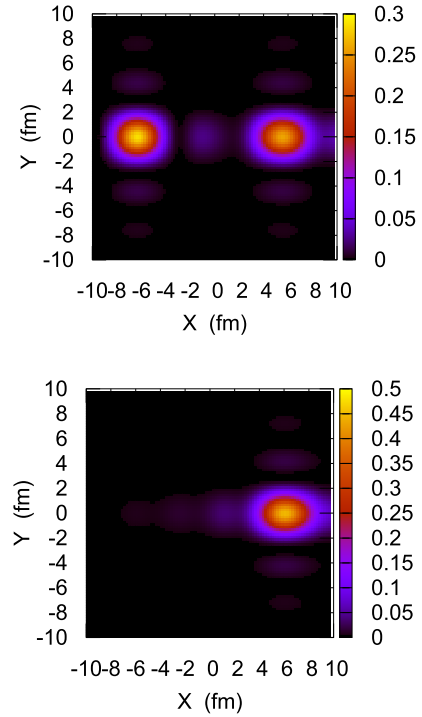**Fig. 3.** The unsymmetrized cross sections for elastic scattering of the ^{16}O+^{16}O (the upper panel) and the ^{18}O+^{18}O (the lower panel) systems. The solid lines show the total cross sections, while the dashed and the dotted lines denote their decompositions into the nearside and the farside components, respectively.

Fig. 4. The images of the unsymmetrized cross sections for elastic scattering of the ^{16}O+^{16}O (the upper panel) and the ^{18}O+^{18}O (the lower panel) systems. The angles in Eq. (1) are set to be $\theta_0 = 55$ degrees and $\Delta\theta = 15$ degrees.

for the ^{18}O+^{18}O system fall off much more rapidly as a function of scattering angle as compared to those for the ^{16}O+^{16}O system. This is most likely due to the surface properties of the optical potentials, that is, the imaginary part has a larger surface diffuseness in the ^{18}O+^{18}O system due to the suraface absorption term, Eq. (6).

We notice that the unsymmetrized cross sections, obtained only with the scattering amplitude $f(\theta)$, show strong oscillations for the ^{16}O+^{16}O system (see the dashed line in the upper panel). This indicates that the effect of symmetrization due to the identical bosons plays a minor role at this energy in the oscillations for the ^{16}O+^{16}O system, even though the small oscillations around $\theta = \pi/2$ for the ^{18}O+^{18}O system are certainly due to the symmetrization of the wave function. To investigate the origin for the oscillations in the ^{16}O+^{16}O, we decompose the scattering amplitude into the nearside and the farside components by using the Legendre functions of the second kind [3]. The solid lines in Fig. 3 show the unsymmetrized cross sections for the ^{16}O+^{16}O (the upper panel) and the ^{18}O+^{18}O (the lower panel) systems, while the dashed and the dotted lines show their decompositions into the nearside and the farside components, respectively. The upper panel indicates that the nearside and the farside components cross each other at around $\theta = 51$ degrees, and the strong oscillations are indeed caused by an interference between the nearside and the farside components. On the other hand, the farside component is largely suppressed in the ^{18}O+^{18}O system due to the strong absorption, and the scattering amplitude is almost solely given by the nearside component. In this way, the quantum coherence observed in the ^{16}O+^{16}O system is decohered in the ^{18}O+^{18}O system due to the couplings to the internal degrees of freedom, that may be regarded as an internal environment.

The images of the unsymmetrized cross sections for the ^{16}O+^{16}O and the ^{18}O+^{18}O systems are shown in the upper and the lower panels of Fig. 4, respectively. These are obtained with $\theta_0 = 55$ degrees and $\Delta\theta = 15$ degrees. Here we set θ_0 close to the crossing point of the nearside and the farside components in the ^{16}O+^{16}O so that both the components contribute with similar magnitudes. For the ^{16}O+^{16}O system, the image has two distinct peaks. The analysis with the nearside and the farside amplitudes indicates that the peak at a positive value of X corresponds to the nearside component while the peak at a negative X corresponds to the farside component. As we have discussed with the Rutherford scattering, the peak of an image corresponds to the

classical impact parameter of scattering. Fig. 4 therefore agrees with the physical picture of the nearside and the farside components, that is, the nearside and the farside components correspond to a positive and a negative impact parameters, respectively. This can also be seen in the ^{18}O+^{18}O system, for which only the nearside component contributes significantly to the cross sections. The image for this system has a peak at a positive value of X, reflecting a positive impact parameter for the nearside component.

In summary, we have proposed a novel way to image nuclear reactions. Based on an idea in wave optics, as had been advocated in the field of particle physics, the image can be obtained by performing Fourier transform of a scattering amplitude. For an angle-independent scattering amplitude, the image is peaked at the origin with the widths determined by parameters in the Fourier transform. For Rutherford scattering, the peak of the image is shifted to the position corresponding to the classical impact parameter of scattering. We have applied this method to elastic scattering of the ^{16}O+^{16}O and ^{18}O+^{18}O systems at energies about 2.6 times the Coulomb barrier. The image for the ^{16}O+^{16}O system has been found to have two peaks, corresponding to the nearside and the farside components of the reaction process. The quantum interference between the two components is largely decohered in the ^{18}O+^{18}O system due to the strong absorption originated from the two extra neutrons outside ^{16}O. The image for this system has been found to have a single peak, corresponding solely to the nearside component. Elastic scattering for the ^{16}O+^{16}O and ^{18}O+^{18}O systems at these energies therefore has close analogies to a double slit and a single slit problems in quantum mechanics, respectively.

In this way, the imaging proposed in this paper provides an intuitive understanding of the origin and the underlying dynamics of quantum interference phenomena in nuclear reactions. Of course, a scattering amplitude is not an observable, unlike cross sections. However, one can make an attempt to fit data with an optical model, from which one can obtain a scattering amplitude to be used for imaging. There are a variety of interference phenomena in nuclear reactions. We leave applications of the imaging to these phenomena for interesting future works.
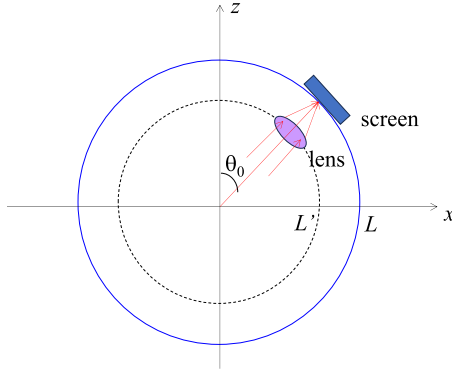
Fig. 5. A schematic view of the set up of a lens and a screen for the imaging. The angle of the lens from the z axis is θ_0 and thus the distance of the lens from the z axis is $L' \sin \theta_0$.

An application to inelastic scattering [18] will be another interesting direction for future works.

Declaration of competing interest

Data availability

Data will be made available on request.

Acknowledgements

**Appendix A. Derivation of Eq. (1)**

In a scattering problem, one considers the asymptotic wave function in a form of

$$\psi(\mathbf{r}) \rightarrow e^{ikz} + f(\theta)\frac{e^{ikr}}{r} \qquad (r \rightarrow \infty), \tag{A1}$$

where $k = \sqrt{2\mu E/\hbar^2}$ is the wave number with E and μ being the energy in the center of mass frame and the reduced mass, respectively. Here we have taken the z-axis for the direction of the incident wave and assumed that the scattering amplitude $f(\theta)$ depends only on the angle θ.

We put a convex lens at the distance L' from the origin in the direction of (θ_0, φ_0) and take an image on the screen located at the distance L from the origin (see Fig. 5). In Fig. 6, the center of the lens is denoted as P', while the center of the screen is denoted as P, both of them are in the direction (θ_0, φ_0) from the origin. We use the two-dimensional Cartesian coordinate systems (ξ, η) and (X_s, Y_s) to express the position of a point on the lens and the screen, respectively. We put the lens in the tangential direction of the sphere at the point P' and take the ξ and the η axis in the $-\theta$ and the φ directions, respectively. ξ and η are then expressed as $\xi \sim -L'(\theta - \theta_0)$ and $\eta \sim (L' \sin \theta_0)(\varphi - \varphi_0)$, respectively, for large values of L'.

We assume that L' is much larger than the size of the lens such that the wave which is incident on the lens can be approximately regarded as a plane wave. The role of the lens is to convert a plane wave to an incoming spherical wave (see Fig. 4 in Ref. [9]). Assuming that the lens
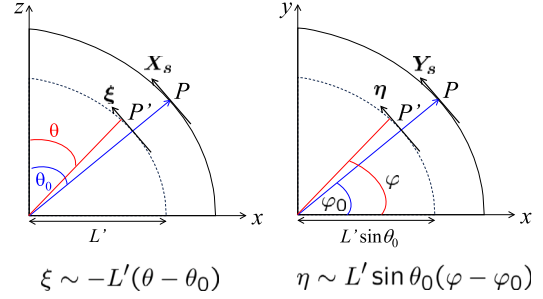
Fig. 6. The definition of the coordinate systems (ξ, η) and (X_s, Y_s) for the imaging. The direction of ξ and X_s is taken to be in the $-\theta$-direction, while the direction of η and Y_s is in the φ-direction.

is infinitely thin, the amplitude at the point (X_s, Y_s) on the screen then reads,

$$\Psi_s(X_s, Y_s) = \int_{-d_\xi}^{d_\xi} d\xi \int_{-d_\eta}^{d_\eta} d\eta \, A(\xi, \eta) e^{-ikr} \tag{A2}$$

where $A(\xi, \eta)$ is the amplitude for the scattering wave at the point (ξ, η) on the lens, and the size of the lens is taken to be $d_\xi \times d_\eta$. $r = [(X_s - \xi)^2 + (Y_s - \eta)^2 + (L - L')^2]^{1/2}$ is the distance between the point at (ξ, η, L') on the lens and the point at (X_s, Y_s, L) on the screen. We further assume that the size of the lens is much smaller than $L - L'$. Eq. (A2) is then transformed to

$$\Psi_s(X_s, Y_s) \sim e^{-ik(L-L')} e^{-ik\frac{X_s^2 + Y_s^2}{2(L-L')}} \int_{-d_\xi}^{d_\xi} d\xi \int_{-d_\eta}^{d_\eta} d\eta \, e^{ik\frac{\xi X_s + \eta Y_s}{L-L'}} A(\xi, \eta). \tag{A3}$$

Using the relations $\xi \sim -L' \sin \theta_0(\theta - \theta_0)$ and $\eta \sim L' \sin \theta_0(\varphi - \varphi_0)$, and by substituting the scattering amplitude $f(\theta)$ to $A(\xi, \eta)$, one finds

$$\Psi_s(X_s, Y_s) \sim e^{-ik(L-L')} e^{-ik\frac{X_s^2 + Y_s^2}{2(L-L')}}$$
$$\times \int_{\theta_0 - \Delta\theta}^{\theta_0 + \Delta\theta} d\theta \int_{\varphi_0 - \Delta\varphi}^{\varphi_0 + \Delta\varphi} d\varphi \, e^{ik\frac{-L'(\theta - \theta_0)X_s + L' \sin \theta_0 Y_s(\varphi - \varphi_0)}{L-L'}} f(\theta), \tag{A4}$$

with $\Delta\theta = d_\xi/L'$ and $\Delta\varphi = d_\eta/(L' \sin \theta_0)$. Introducing scaled coordinates $X \equiv -L' X_s/(L - L')$ and $Y \equiv L' \sin \theta_0 Y_s/(L - L')$, one finally obtains Eq. (1), up to a phase factor. Notice that the relation $\Delta\varphi = \Delta\theta/\sin \theta_0$ holds for a square lens, $d_\xi = d_\eta$.

Appendix B. The image of Rutherford scattering

We evaluate the image in the X direction,

$$\Phi(X) = \int_{\theta_0 - \Delta\theta}^{\theta_0 + \Delta\theta} d\theta \, e^{ik(\theta - \theta_0)X} f(\theta), \tag{B1}$$

for small values of $\Delta\theta$. To this end, we expand $e^{ik(\theta - \theta_0)X}$ and $f(\theta)$ around $\theta = \theta_0$ up to the second order:

$$e^{ik(\theta - \theta_0)X} \sim 1 + ik(\theta - \theta_0)X - k^2 X^2(\theta - \theta_0)^2/2, \tag{B2}$$
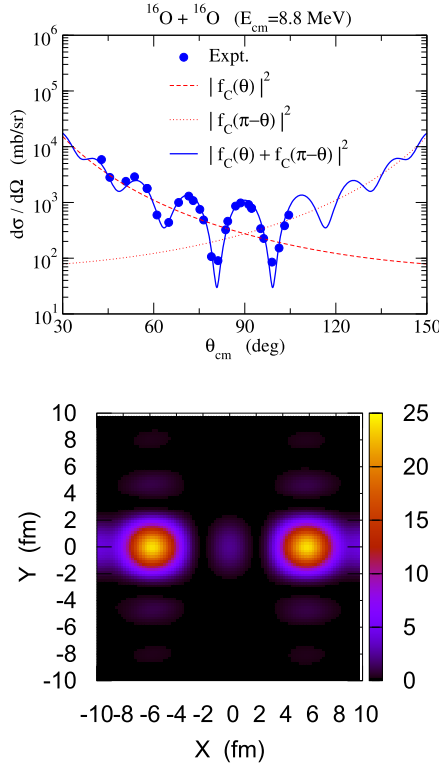
$$f(\theta) \sim f(\theta_0) + f'(\theta_0)(\theta - \theta_0) + f''(\theta_0)(\theta - \theta_0)^2/2. \tag{B3}$$

The integral in Eq. (B1) can then be performed easily and reads,

$$\Phi(X) \sim 2\Delta\theta \left\{ f(\theta_0) + \frac{(\Delta\theta)^2}{3} \left(-\frac{k^2 X^2}{2} f(\theta_0) + ikX f'(\theta_0) + \frac{f''(\theta_0)}{2} \right) \right\}. \tag{B4}$$

From this equation, one obtains

Fig. 7. (Upper panel) The differential cross sections for elastic scattering of ^{16}O$+^{16}$O at $E_{c.m.} = 8.8$ MeV. The contributions of unsymmetrized scattering amplitudes are also shown by the dashed and the dotted lines. The experimental data are taken from Ref. [1]. (Lower panel) The image of Mott scattering shown in the upper panel. θ_0 and $\Delta\theta$ are taken to be 90 and 30 degrees, respectively.

$$\frac{d}{dX}|\Phi(X)|^2 \propto -2k^2|f(\theta_0)|^2 X$$
$$+ik(f^*(\theta_0)f'(\theta_0) - f(\theta_0)f'(\theta_0)^*). \tag{B5}$$

The peak of the image then appears at

$$X = \frac{i}{2k}\left(\frac{f'(\theta_0)}{f(\theta_0)} - \frac{f'(\theta_0)^*}{f^*(\theta_0)}\right). \tag{B6}$$

We apply this to Rutherford scattering, whose scattering amplitude is given by,

$$f_C(\theta) = -\frac{\eta}{2k\sin^2\frac{\theta}{2}}\exp\left[-i\eta\ln\left(\sin^2\frac{\theta}{2}\right) + 2i\sigma_0\right]. \tag{B7}$$

Here, $\eta = Z_1 Z_2 e^2/\hbar v$ is the Sommerfeld parameter, where v is the relative velocity, and $\sigma_0 = \arg\Gamma(1 + i\eta)$ is the s-wave Coulomb phase shift. For Eq. (B7), one finds

$$\frac{f'_C(\theta)}{f_C(\theta)} = -(1 + i\eta)\cot\left(\frac{\theta}{2}\right). \tag{B8}$$

The peak of the image therefore appears at

$$X = \frac{\eta}{k}\cot\left(\frac{\theta_0}{2}\right), \tag{B9}$$

that is nothing but the impact parameter for Rutherford scattering.

Appendix C. The image of Mott scattering

Let us consider Mott scattering, i.e., scattering of two identical particles, for which the scattering amplitude is given by $f(\theta) \pm f(\pi - \theta)$. For the component $f(\pi - \theta)$, the X dependence of Eq. (1) reads

$$\Phi_{\pi-\theta}(X) \equiv \int_{\theta_0-\Delta\theta}^{\theta_0+\Delta\theta} d\theta\, e^{ik(\theta-\theta_0)X} f(\pi - \theta) \tag{C1}$$

$$= \int_{\pi-\theta_0-\Delta\theta}^{\pi-\theta_0+\Delta\theta} d\tilde{\theta}\, e^{ik(\pi-\tilde{\theta}-\theta_0)X} f(\tilde{\theta}), \tag{C2}$$

where $\tilde{\theta}$ is defined as $\tilde{\theta} = \pi - \theta$. For $\theta_0 = \pi/2$, this is equivalent to

$$\Phi_{\pi-\theta}(X) = \int_{\theta_0-\Delta\theta}^{\theta_0+\Delta\theta} d\tilde{\theta}\, e^{ik(\theta_0-\tilde{\theta})X} f(\tilde{\theta}) = \Phi_\theta(-X). \tag{C3}$$

Thus, the image of Mott scattering is symmetric with respect to $X = 0$, and it therefore has two symmetric peaks at X_{peak} and $-X_{peak}$.

The upper panel of Fig. 7 shows the differential cross sections for elastic scattering of ^{16}O$+^{16}$O at $E_{c.m.} = 8.8$ MeV. This energy is at about 1.5 MeV below the Coulomb barrier, and the nuclear effect can be neglected. In fact, the experimental data can be well fitted using the Coulomb scattering amplitudes, $d\sigma/d\Omega = |f_C(\theta) + f_C(\pi - \theta)|^2$. The contributions of $f_C(\theta)$ and $f_C(\pi - \theta)$ are also shown by the dashed and the dotted lines, respectively. The image of Mott scattering is shown in the lower panel. θ_0 and $\Delta\theta$ are taken to be 90 and 30 degrees, respectively. As we have argued, the image has two symmetric peaks. A comparison with Fig. 1 indicates that the peak at a positive X corresponds to the contribution of $f_C(\theta)$, while the peak at a negative X corresponds to the contribution of $f_C(\pi - \theta)$.

References

[1] D.A. Bromley, J.A. Kuehner, E. Almqvist, Elastic scattering of identical spin-zero nuclei, Phys. Rev. 123 (1961) 878–893, https://doi.org/10.1103/PhysRev.123.878, https://link.aps.org/doi/10.1103/PhysRev.123.878.

[2] D.M. Brink, Semi-Classical Methods for Nucleus-Nucleus Scattering, Cambridge Monographs on Mathematical Physics, Cambridge University Press, 1985, https://books.google.co.jp/books?id=zmdUMSXKIkgC.

[3] R.C. Fuller, Qualitative behavior of heavy-ion elastic scattering angular distributions, Phys. Rev. C 12 (1975) 1561–1574, https://doi.org/10.1103/PhysRevC.12.1561, https://link.aps.org/doi/10.1103/PhysRevC.12.1561.

[4] N. Rowley, C. Marty, Saddles and trajectories, and poles and surface waves in heavy-ion elastic scattering, Nucl. Phys. A 266 (2) (1976) 494–520, https://doi.org/10.1016/0375-9474(76)90371-7, https://www.sciencedirect.com/science/article/pii/0375947476903717.

[5] M. Hussein, K. McVoy, Nearside and farside: the optics of heavy ion elastic scattering, Prog. Part. Nucl. Phys. 12 (1984) 103–170, https://doi.org/10.1016/0146-6410(84)90003-6, https://www.sciencedirect.com/science/article/pii/0146641084900036.

[6] D. Brink, N. Takigawa, Barrier penetration effects in the semi-classical theory of elastic scattering between complex nuclei, Nucl. Phys. A 279 (1) (1977) 159–188, https://doi.org/10.1016/0375-9474(77)90427-4, https://www.sciencedirect.com/science/article/pii/0375947477904274.

[7] K. Hashimoto, Y. Matsuo, T. Yoda, String is a double slit, Prog. Theor. Exp. Phys. 2023 (4) (2023) 043B04, https://doi.org/10.1093/ptep/ptad045.

[8] K. Hashimoto, S. Kinoshita, K. Murata, Einstein rings in holography, Phys. Rev. Lett. 123 (2019) 031602, https://doi.org/10.1103/PhysRevLett.123.031602, https://link.aps.org/doi/10.1103/PhysRevLett.123.031602.

[9] K. Hashimoto, S. Kinoshita, K. Murata, Imaging black holes through the AdS/CFT correspondence, Phys. Rev. D 101 (2020) 066018, https://doi.org/10.1103/PhysRevD.101.066018, https://link.aps.org/doi/10.1103/PhysRevD.101.066018.

[10] K. Konishi, G. Paffuti, Quantum Mechanics: A New Introduction, OUP Oxford, 2009, https://books.google.co.jp/books?id=33RdDgAAQBAJ.

[11] R.H. Siemssen, J.V. Maher, A. Weidinger, D.A. Bromley, Excitation-function structure in O^{16}+O^{16} scattering, Phys. Rev. Lett. 19 (1967) 369–372, https://doi.org/10.1103/PhysRevLett.19.369, https://link.aps.org/doi/10.1103/PhysRevLett.19.369.

[12] R. Vandenbosch, W. Reisdorf, P. Lau, Elastic and inelastic scattering of 18O by 16O and 18O, Nucl. Phys. A 230 (1) (1974) 59–69, https://doi.org/10.1016/0375-9474(74)90529-6, https://www.sciencedirect.com/science/article/pii/0375947474905296.

[13] Y. Kondō, B. Robson, R. Smith, A deep potential description of the 16O+16O system, Phys. Lett. B 227 (3) (1989) 310–314, https://doi.org/10.1016/0370-2693(89)90935-0, https://www.sciencedirect.com/science/article/pii/0370269389909350.

[14] S. Ohkubo, K. Yamashita, Evidence for ^{16}O $+ ^{16}$O cluster bands in ^{32}S, Phys. Rev. C 66 (2002) 021301, https://doi.org/10.1103/PhysRevC.66.021301, https://link.aps.org/doi/10.1103/PhysRevC.66.021301.

[15] R.W. Shaw, R. Vandenbosch, M.K. Mehta, Elastic scattering of ^{18}O by ^{18}O, Phys. Rev. Lett. 25 (1970) 457–461, https://doi.org/10.1103/PhysRevLett.25.457, https://link.aps.org/doi/10.1103/PhysRevLett.25.457.

[16] C. Von Charzewski, V. Hnizdo, C. Toepffer, Symmetry and shell effects in heavy-ion scattering, Nucl. Phys. A 307 (2) (1978) 309–318, https://doi.org/10.1016/0375-9474(78)90620-6, https://www.sciencedirect.com/science/article/pii/0375947478906206.

[17] F. Haas, Y. Abe, Surface transparency and resonant behavior in some lighter-heavy-ion reactions, Phys. Rev. Lett. 46 (1981) 1667–1670, https://doi.org/10.1103/PhysRevLett.46.1667, https://link.aps.org/doi/10.1103/PhysRevLett.46.1667.

[18] D.R. Dean, N. Rowley, Nearside-farside analysis of inelastic heavy-ion scattering, J. Phys. G 10 (4) (1984) 493, https://doi.org/10.1088/0305-4616/10/4/011, https://dx.doi.org/10.1088/0305-4616/10/4/011.